Shallow Gas: Rock Physics and AVO

Appendices

Universiteit Utrecht

Martijn M.T.G. Janssen

June 2015

Student number – 4139194
(F120805)

Master Thesis – GEO4-1520

Supervisors:
M. Boogaard, van den (EBN)
H.L.J.G. Hoetz (EBN)
Prof. dr. J.A. Trampert (UU)

Contents

1.Appendices full-stack data observations

Appendix A: Seismic sections through the observed amplitude anomalies

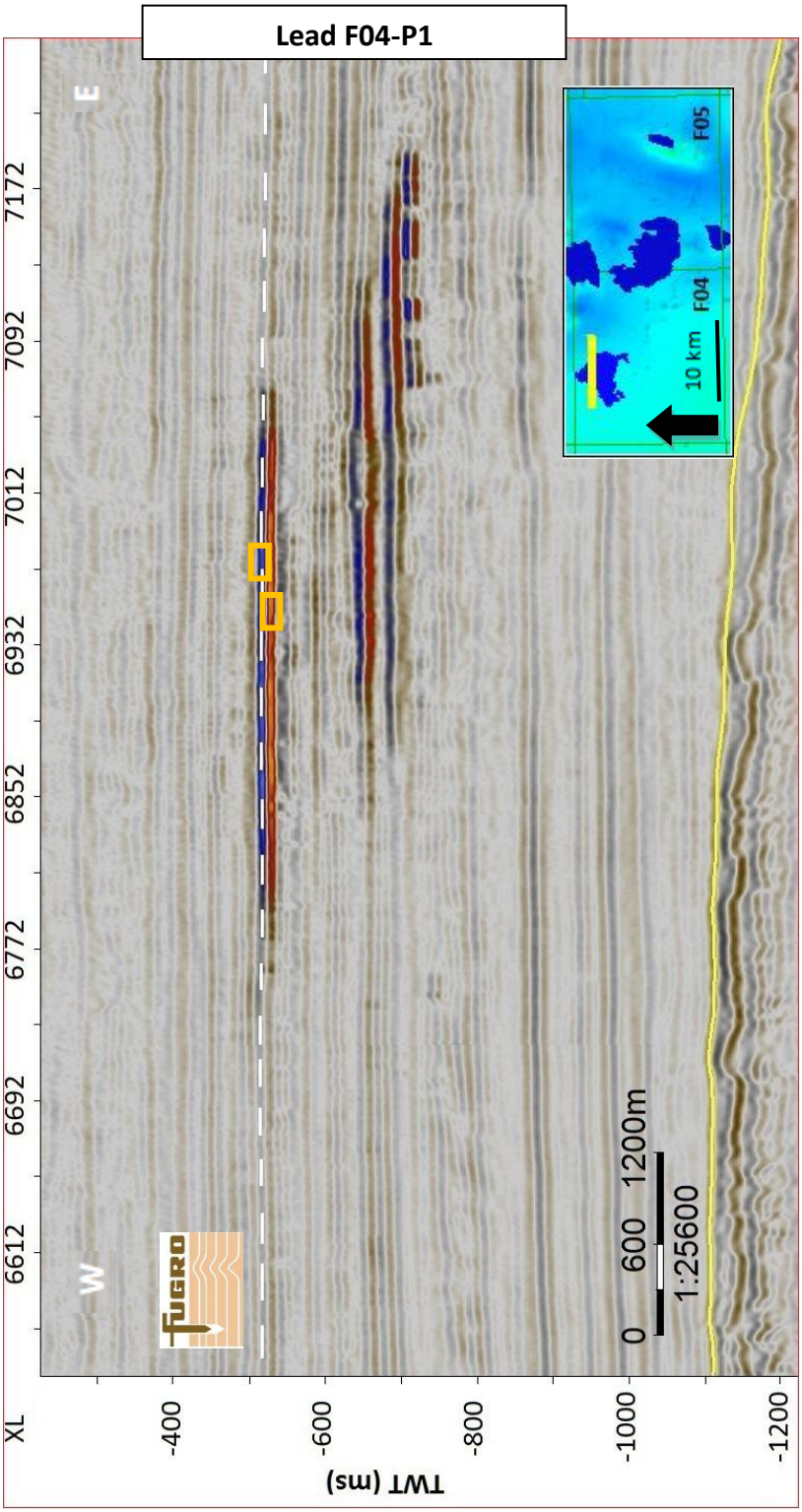

Figure 1: Seismic line through lead F04-P1 (anomaly 1). The yellow line represents the Mid-Miocene Unconformity (MMU). Note the multiple stacked reservoirs and the absence of a clear phase reversal. The reflector of interest, used for AVO analysis, is marked by the white dashed line. The lower right figure presents the location of the line within the study area: colors specify the depth to the MMU where blue represent greater depths. The polygons in blue present the five identified anomalies. The areas which have been used to analyze the AVO behavior of the top- and bottom-reservoir reflector in figure 7.4 are shown in yellow.

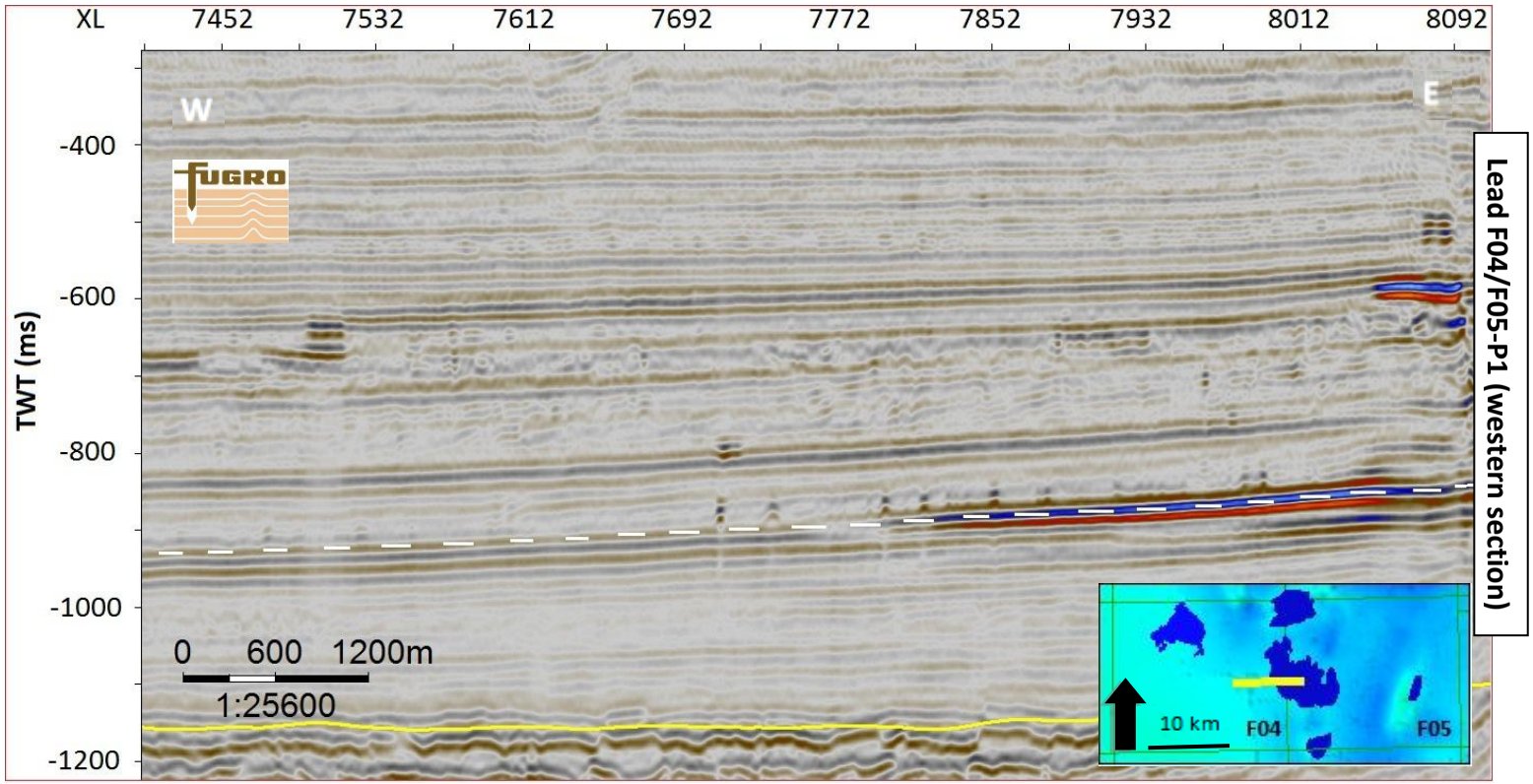

Figure 2: Seismic line through the western part of lead F04/F05-P1 (anomaly 3). The yellow line represents the Mid-Miocene Unconformity (MMU). Note the multiple stacked reservoirs and the phase reversal at a crossline of ~7772. The reflector of interest, used for AVO analysis, is marked by the white dashed line. The lower right figure presents the location of the line within the study area: colors specify the depth to the MMU where blue represent greater depths. The polygons in blue present the five identified anomalies.

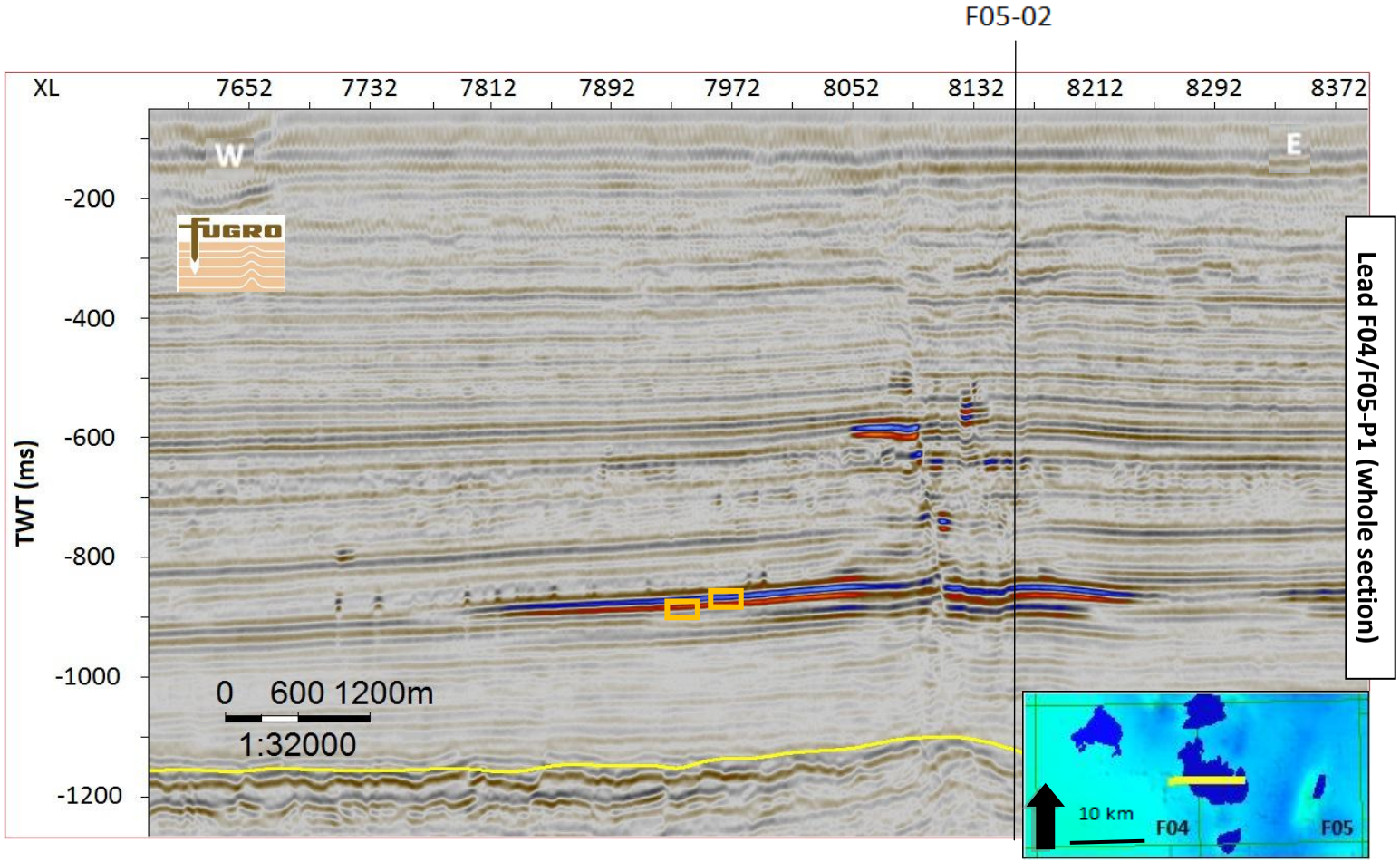

Figure 3: Seismic line through lead F04/F05-P1 (anomaly 3). The yellow line represents the Mid-Miocene Unconformity (MMU). Note the multiple stacked reservoirs and the phase reversals at crosslines of ~7772 and ~8212. The lower right figure presents the location of the line within the study area: colors specify the depth to the MMU where blue represent greater depths. The polygons in blue present the five identified anomalies. The areas which have been used to analyze the AVO behavior of the top- and bottom-reservoir reflector in figure 7.4 are shown in yellow.

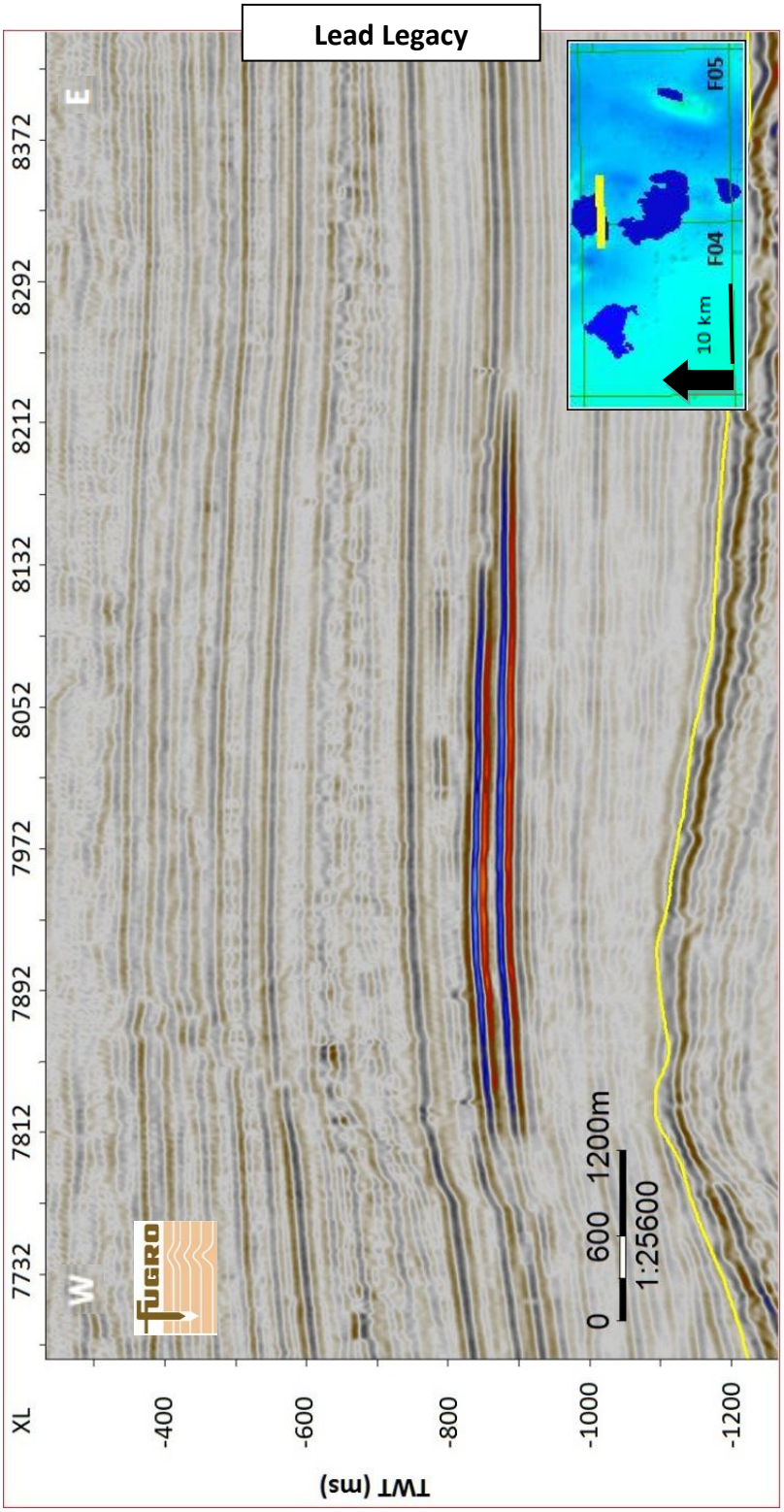

Figure 4: Seismic line through lead Legacy (anomaly 2). The yellow line represents the Mid-Miocene Unconformity (MMU). Note the multiple stacked reservoirs and the phase reversal at a crossline of ~8212. The lower right figure presents the location of the line within the study area: colors specify the depth to the MMU where blue represent greater depths. The polygons in blue present the five identified anomalies.

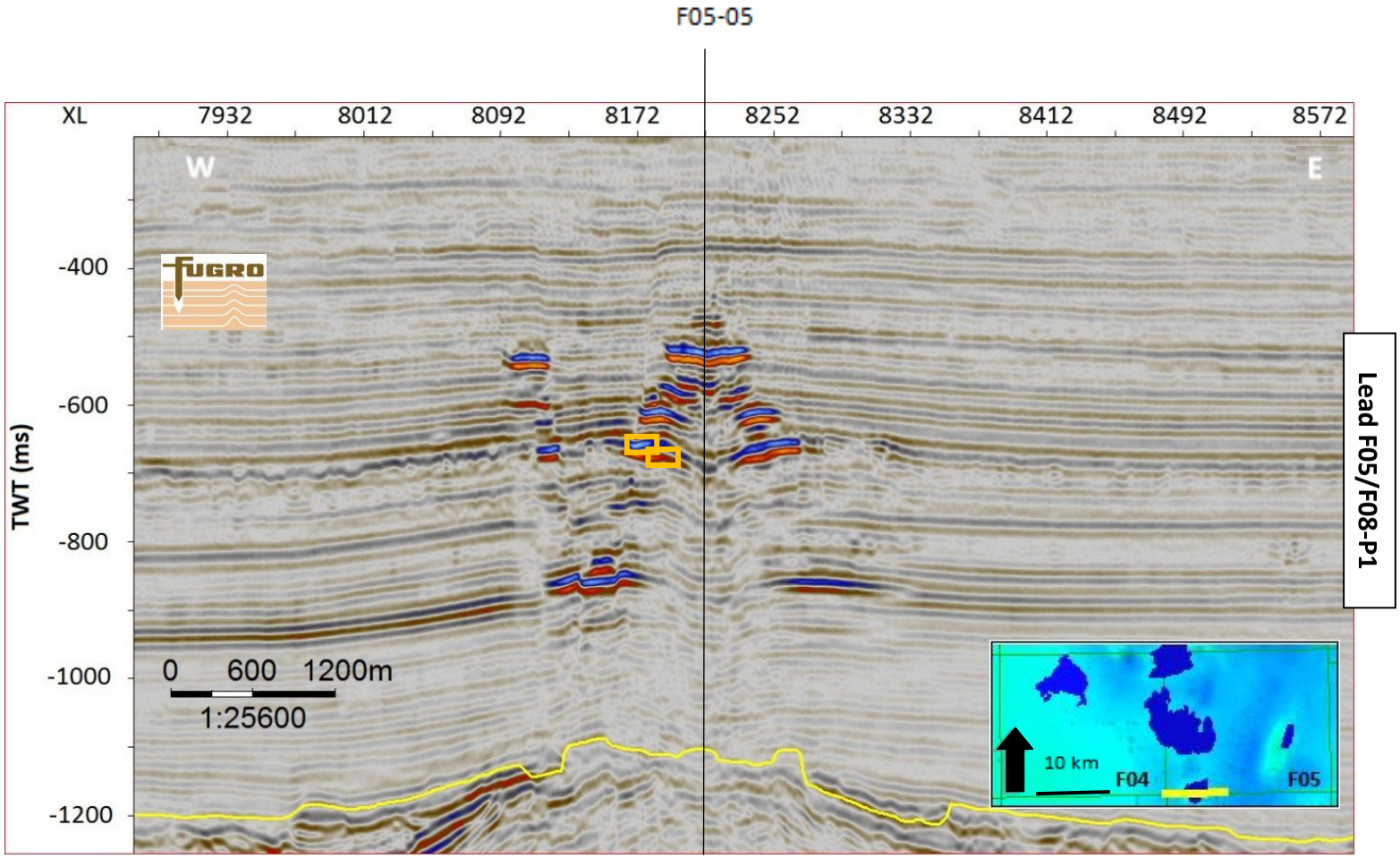

Figure 5: Seismic line through lead F05/F08-P1 (anomaly 4). The yellow line represents the Mid-Miocene Unconformity (MMU). Note the multiple stacked reservoirs and the absence of a clear phase reversal. The anomaly is directly located above a salt dome. The lower right figure presents the location of the line within the study area: colors specify the depth to the MMU where blue represent greater depths. The polygons in blue present the five identified anomalies. The location of well F05-05 is also shown. The areas which have been used to analyze the AVO behavior of the top- and bottom-reservoir reflector in figure 7.4 are shown in yellow.

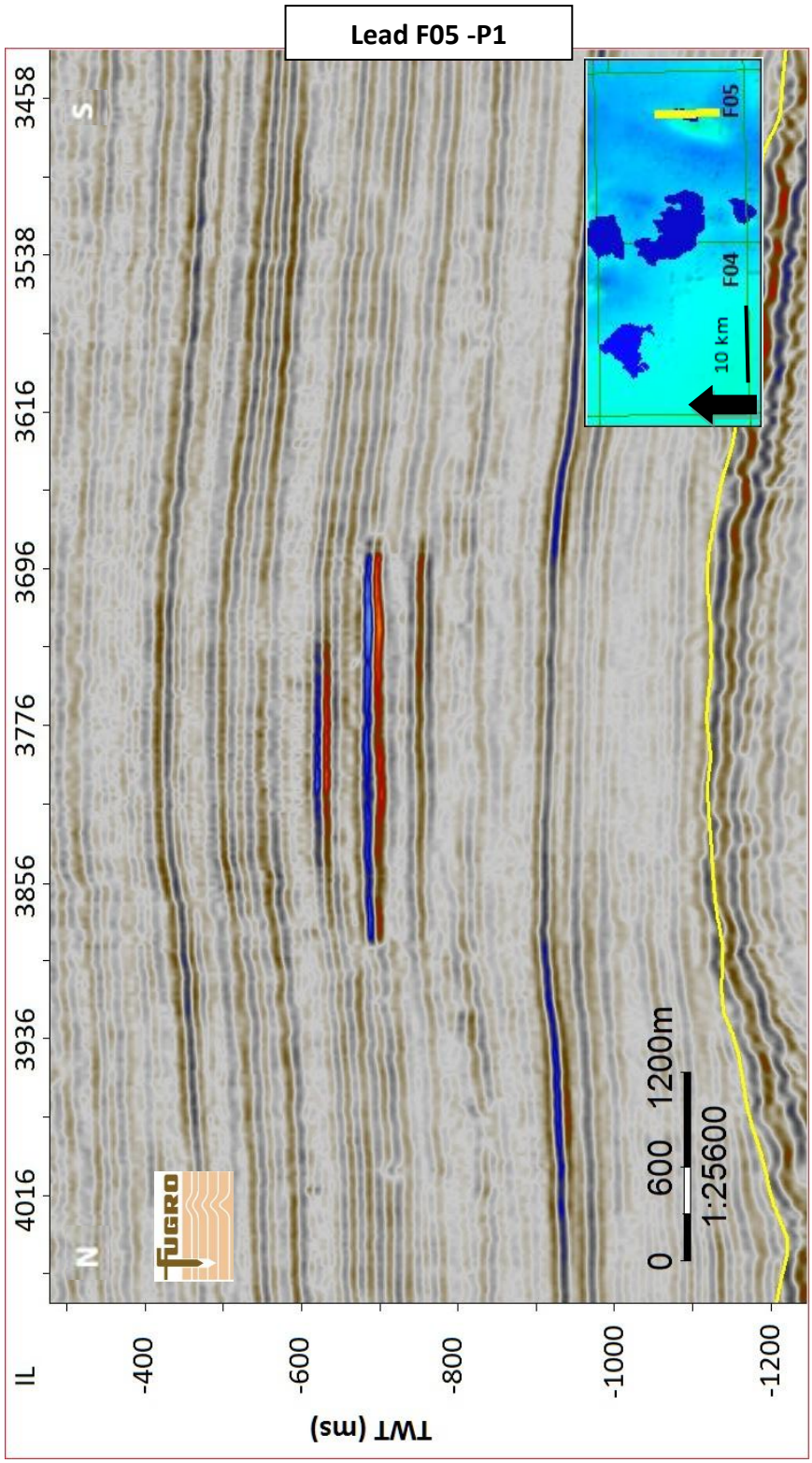

Figure 6: Seismic line through lead F05-P1 (anomaly 5). The yellow line represents the Mid-Miocene Unconformity (MMU). Note the multiple stacked reservoirs and phase reversals at inlines ~3890 and ~3686. The lower right figure presents the location of the line within the study area: colors specify the depth to the MMU where blue represent greater depths. The polygons in blue present the five identified anomalies.

- *Note that the seismic lines in this appendix contain the EU polarity convention where an increasing impedance represent negative (red) amplitudes. The reflectors of interest (figures 1 and 2) are used in section 7.2.*

2.Appendices petrophysical analysis

Appendix B: Schematic cross section of well F04-01: measured depth versus true vertical depth subsea.

The figure below presents a schematic cross section of well F04-01.

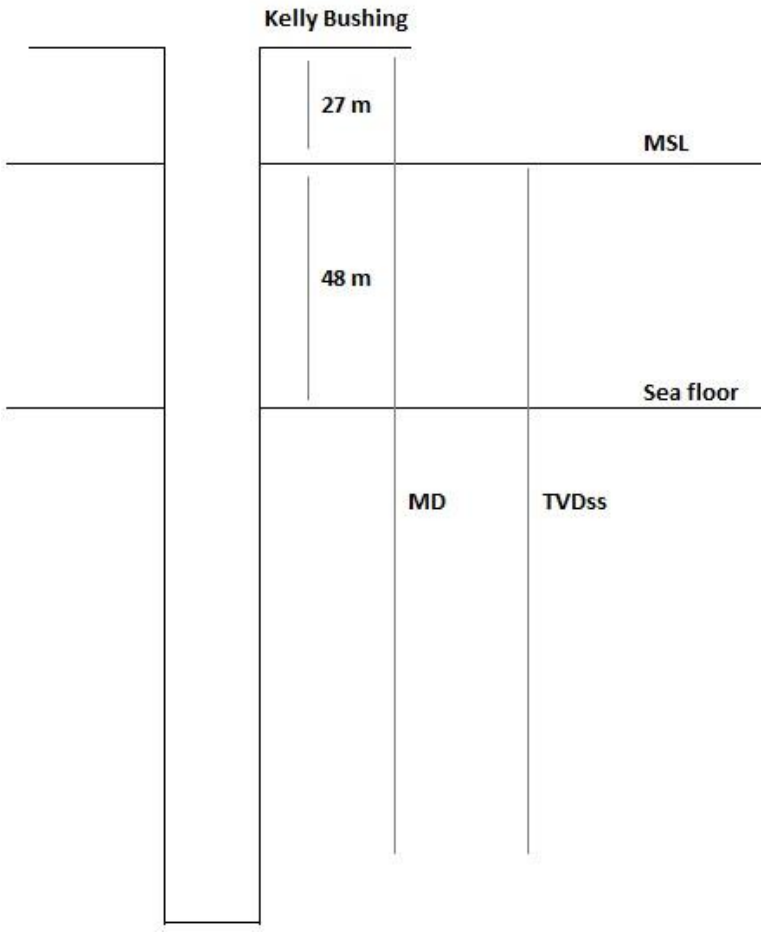

Figure 7: A schematic cross section of well F04-01. MSL, MD and TVDss represent respectively the mean sea level, measured depth and the true vertical depth subsea.

Note that well F04-01 has been drilled vertically through the shallow subsurface. The measured depth refers to the depth with respect to the level of the kelly bushing above the water surface. The true vertical depth subsea uses the mean sea level as a reference.

Appendix C: Well analysis

- Depths in m (MD) - na = not available - Expl. = Exploration Well

Well	GR		DT		RHOB		DRHO		NPHI		Resistivity		SP	
	from	*to*	*from*	*to*	*from*	*to*	*from*	*to*	*from*	*to*	*from*	*to*	*from*	*to*
F04-01	76.3 m	3121.4 m	391.4 m	3129.6 m	1750.2 m	2874.6 m	1750.2 m	2874.6 m	na	na	1288.1 m	2039.9 m	386.0 m	1083.0 m
F04-02-A	480.1 m	4645.9 m	490.1 m	4639.8 m	1956.2 m	4648.8 m	1956.2 m	4648.8 m	1956.3 m	4644.9 m	na	na	na	na
F04-03	31.1 m	4534.0 m	456.0 m	4540.3 m	3701.3 m	4547.4 m	3701.3 m	4547.4 m	3358.0 m	4542.0 m	na	na	na	na
F05-01	108.3 m	2935.6 m	304.2 m	2935.1 m	1800.0 m	2994.2 m	1800.0 m	2994.2 m	1800.2 m	2926.7 m	1800.0 m	2926.8 m	300.3 m	1400.1 m
F05-02	90.5 m	2866.0 m	410.1 m	2860.4 m	1495.0 m	2869.8 m	na	na	1495.2 m	2869.6 m	na	na	na	na
F05-03	79.5 m	2899.6 m	764.1 m	2896.6 m	2108.0 m	2900. 9 m	2108.0 m	2900.9 m	2108.0 m	2900.9 m	766.6 m	2892.9 m	79.4 m	2908.9 m
F05-04	70.7 m	1440.1 m	521.0 m	1429.5 m	510. 6 m	1444.1 m	510. 6 m	1444.1 m	510.7 m	1444.3 m	154.4 m	512.6 m	70.4 m	557.3 m
F05-05	20.6 m	1749.8 m	1033.3 m	1763.5 m	1509.7 m	1750.6 m	1509.7 m	1750.6 m	1509.7 m	1750.6 m	1036.5 m	1555.9 m	1036.5 m	1555.9 m

Well	Age	Type	Target	Useful logs	Result	Remarks
F04-01	1971	Expl.	Lower Triassic Bunter sandstones	3	dry	Additional drilling data show sand intervals between 0-1000m depth.
F04-02-A	1980	Expl.	Rotliegendes sandstones (+ Zechstein carbonates)	2	dry	-
F04-03	1992	Expl.	Upper Carboniferous sandstones and conglomerates	2	dry	Sand body identified at a measured depth of ~792 m seems to contain some gas.
F05-01	1975	Expl.	Upper & Lower Dogger (+ Cretaceous sands)	3	dry	sand body identified at a measured depth of ~350 m.
F05-02	1982	Expl.	Upper Cretaceous Chalk (+ Bunter sandstones)	2	dry	sand body identified at a measured depth of ~450 m seems to contain some gas.
F05-03	1987	Expl.	Upper Jurassic Upper & Lower Graben sandstones	5	dry	sand body identified at a measured depth of ~980 m seems to contain some gas.
F05-04	1998	Expl.	Ekofisk Chalk formation	7	oil shows in the Ekofisk formation (1350 m depth)	sand body identified at a measured depth of ~450 m. + 'Gassand' layer at a measured depth of ~931 m.
F05-05	2001	Expl.	Ekofisk & Ommelanden Chalk formation	1	dry	sand body identified at a measured depth of ~450 m.

Appendix D: Gamma ray data well F05-04

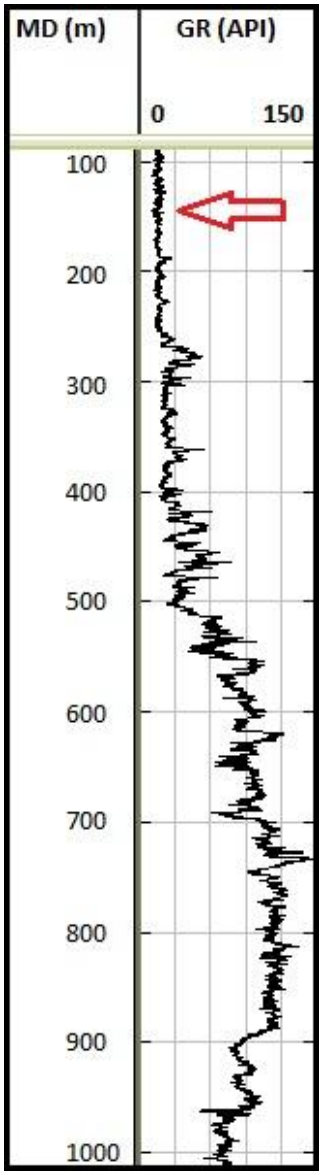

Figure 8: Gamma ray data corresponding to well F05-04. The red arrow presents the reference GR response for quartz.

Figure 8 presents the gamma ray data which is available for well F05-04. The gamma ray response corresponding to quartz is assumed to be 20 API since clean sand intervals were observed by the wellsite geologist between 100-200 m depth (MD).

Appendix E: Derivation of shale parameters (DT, RHOB and GR) for well F05-04

For NPHI, a value of 0.5 has been assumed corresponding to shale (Crain, 2000). With this insight, the other parameters are derived using the following cross plots:

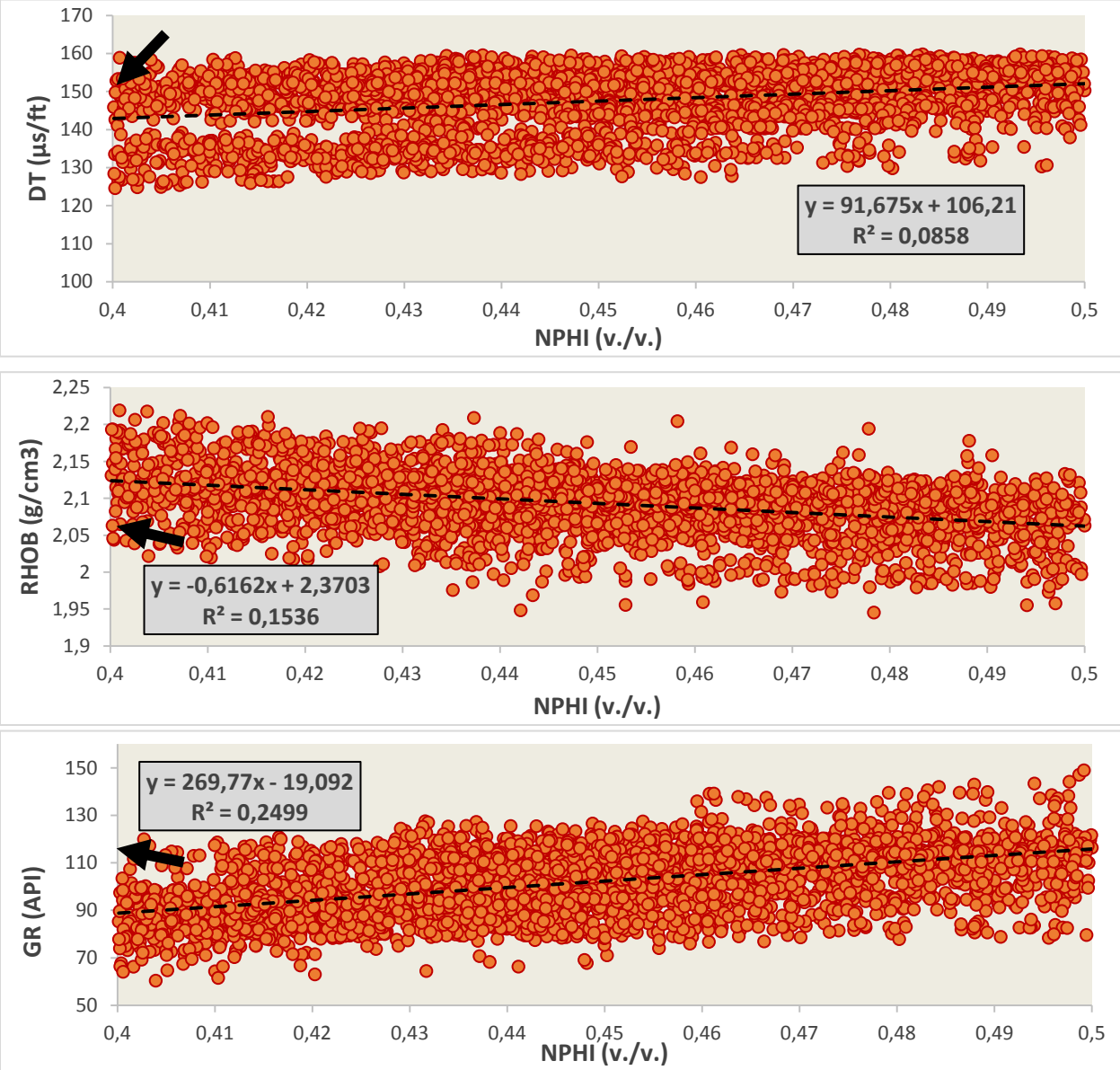

Figure 9: The cross plots that are used to derive shale parameters for the petrophysical analysis of well F05-04.

- **For DT, a value of 150 µs/ft has been assumed.**
- **For RHOB, a value of 2.06 g/cm^3 has been assumed.**
- **For GR, a value of 115 API has been assumed.**

Appendix F: Derivation of the Vp-ρ relationship in well F05-04

In order to establish this relationship, the whole depth interval of 550-1000 m (MD) has been used. The results are presented in figure 10.

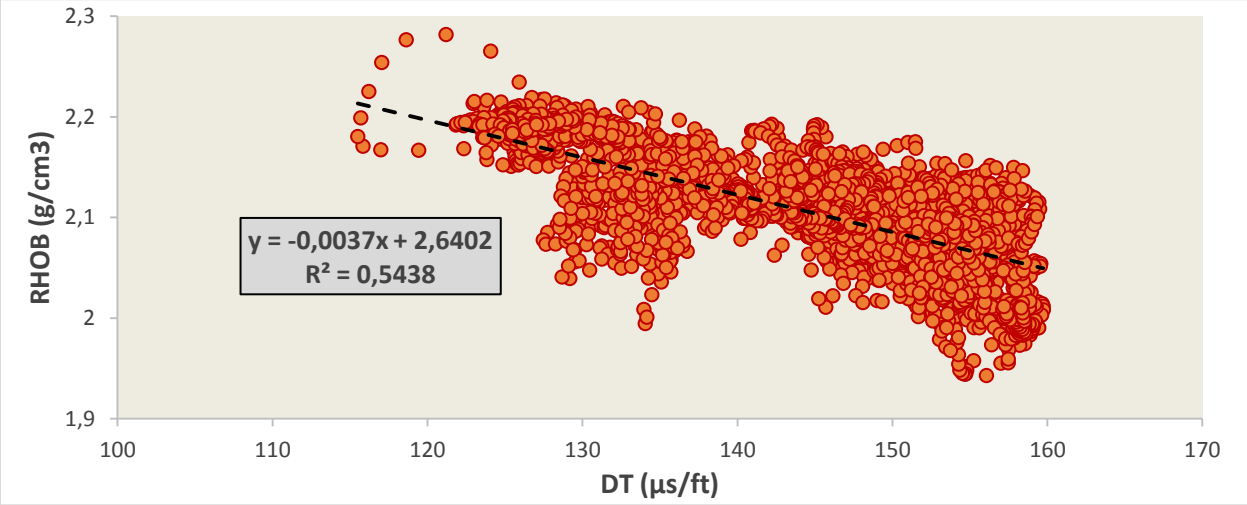

Figure 10: The derived Vp-ρ relationship that is used to predict density values corresponding to wells F04-01 and F05-01.

Appendix G: F04-01 well data used in the petrophysical analysis

Figure 11 shows the well log data that is used in the petrophysical analysis of well F04-01.

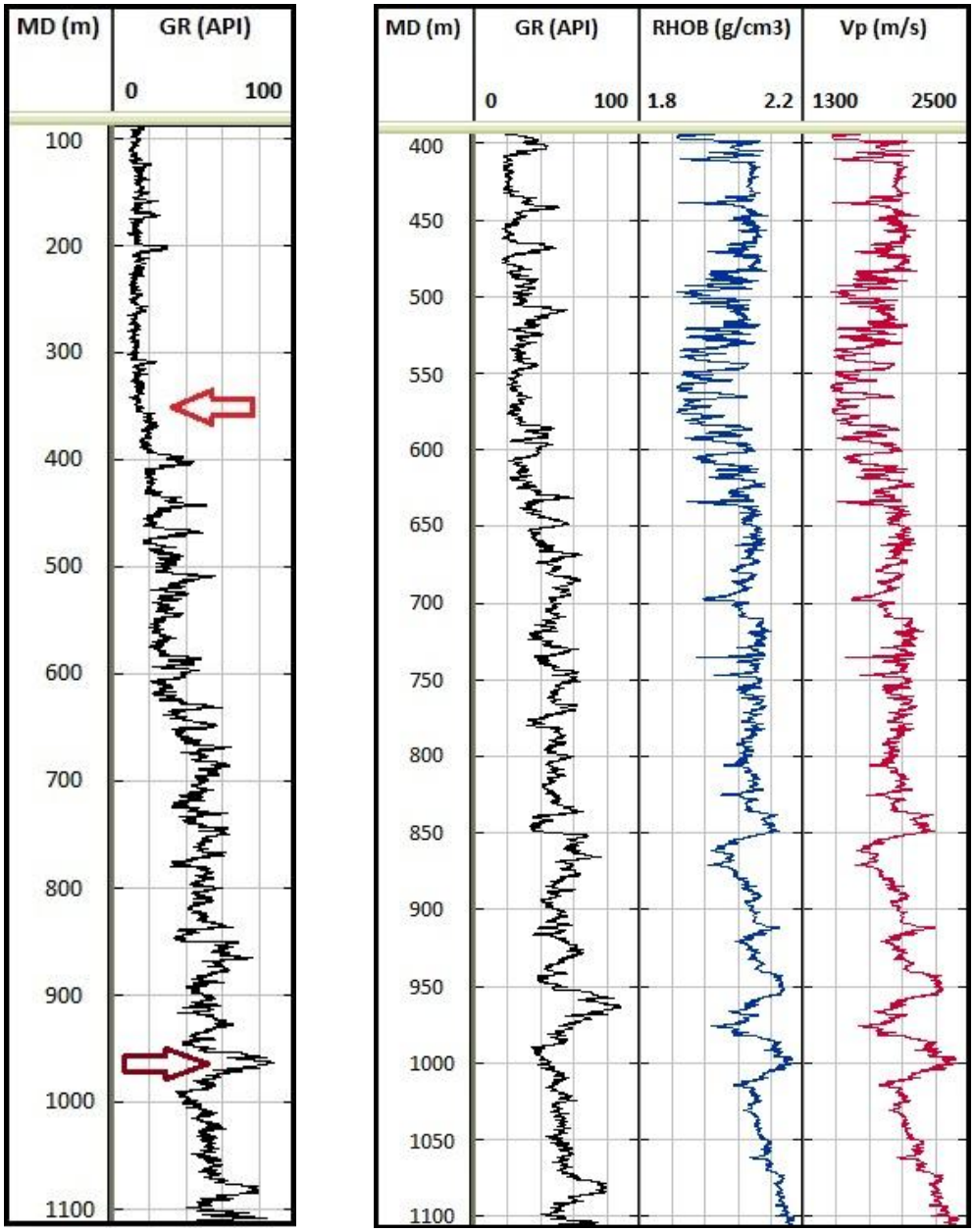

Figure 11: Right: the well data that is used for the petrophysical analysis of well F04-01. Note that density data has been derived from the V_p-ρ relationship of well F05-04. Left: the gamma ray log for the whole interval. The red and brown arrow represent respectively the GR response for quartz (20 API) and for shale (85 API).

Based on the observations of the wellsite geologist, gamma ray responses for quartz and shale are assumed.

Appendix H: F05-01 well data used in the petrophysical analysis

Figure 12 shows the well log data that is used in the petrophysical analysis of well F05-01.

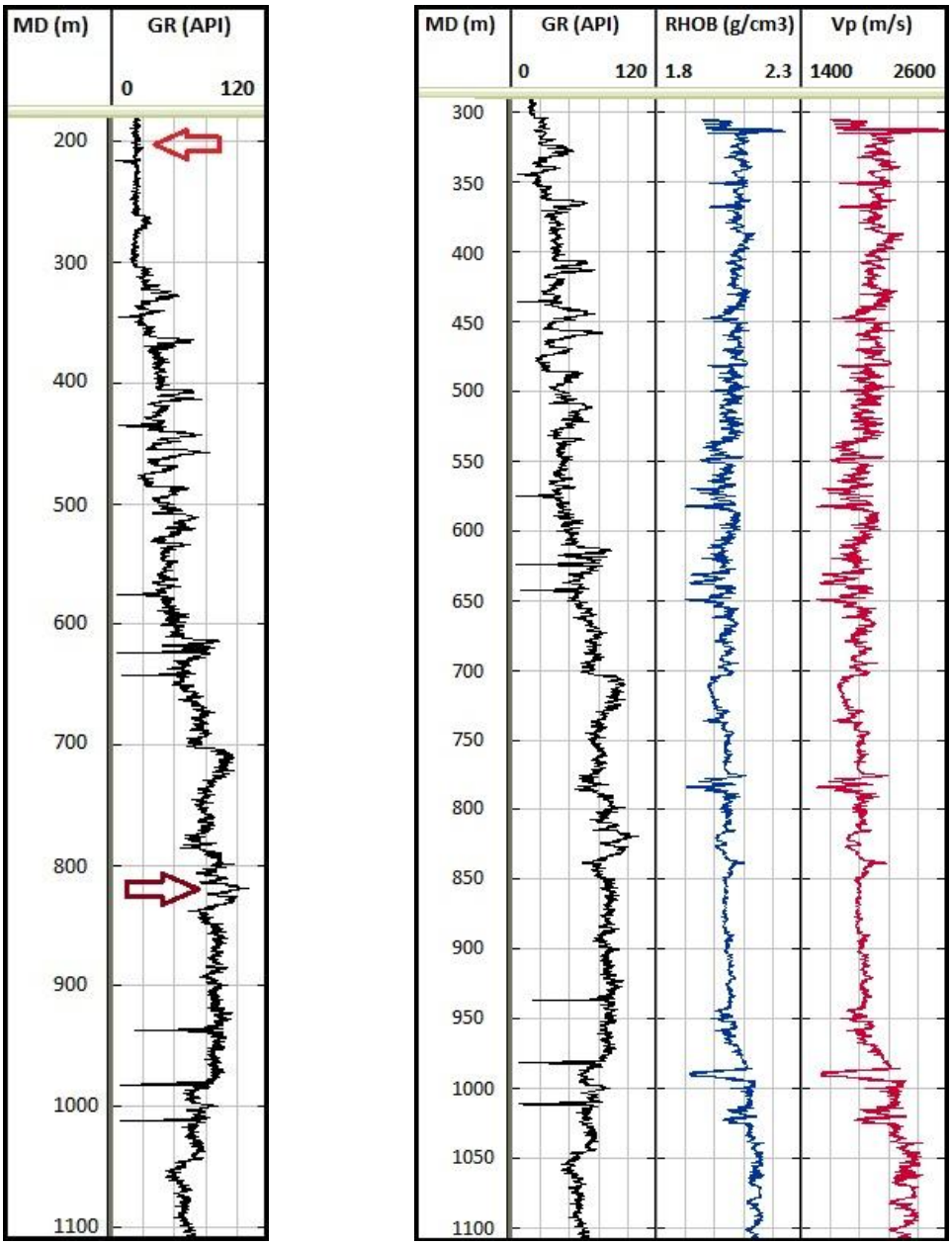

Figure 12: Right: the well data that is used for the petrophysical analysis of well F05-01. Note that density data has been derived from the V_P-ρ relationship of well F05-04. The spikes in the gamma ray data may be the result of measurement failures. Left: the gamma ray log for the whole interval. The red and brown arrow represent respectively the GR response for quartz (20 API) and for shale (95 API).

Based on the observations of the wellsite geologist, gamma ray responses for quartz and shale are assumed.

Appendix I: Derivation of shale parameters (DT and RHOB) for well F04-01

Since this well does not contain any NPHI data, GR data has been chosen as a criteria to identify shale. Additional well data (e.g. composite well logs) show a GR response of 85 API corresponding to shale (see appendix G). With this insight, the other parameters are derived using the following cross plots:

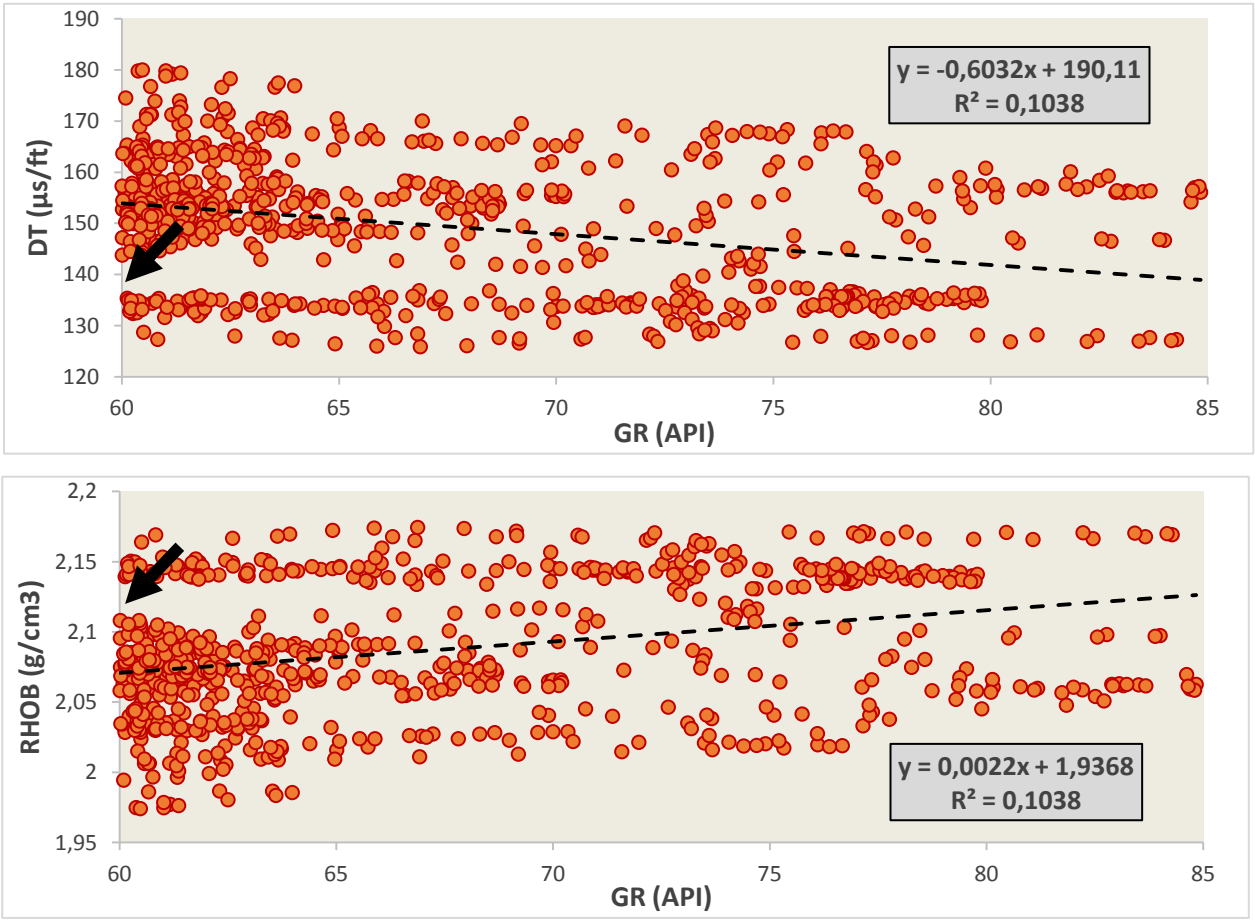

Figure 13: The cross plots that are used to derive shale parameters for the petrophysical analysis of well F04-01.

- **For DT, a value of 139 µs/ft has been assumed.**
- **For RHOB, a value of 2.12 g/cm^3 has been assumed.**

Appendix J: Derivation of shale parameters (DT and RHOB) for well F05-01

Since this well does not contain any NPHI data, GR data has been chosen as a criteria to identify shale. A GR response of 95 API has been used as a reference for shale (see appendix H). The other parameters are obtained using the following cross plots:

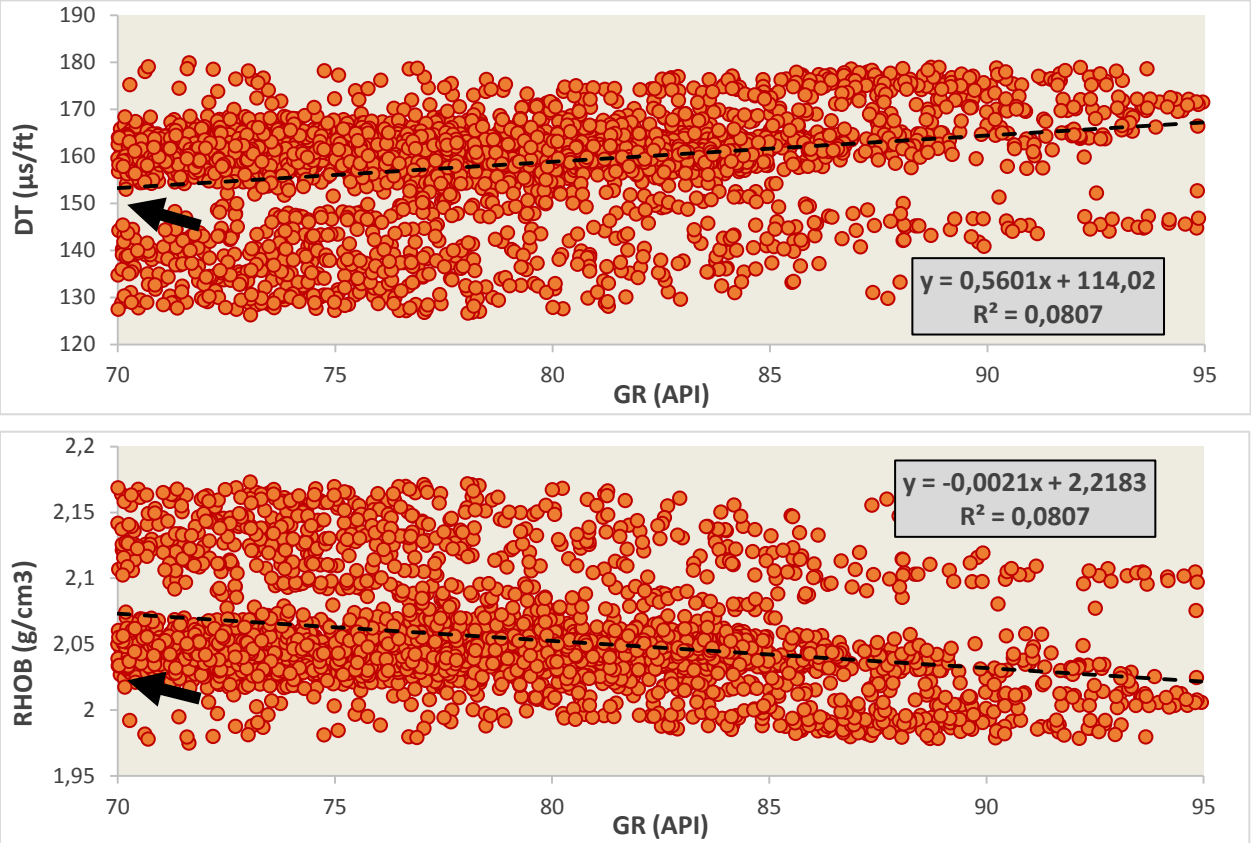

Figure 14: The cross plots that are used to derive shale parameters for the petrophysical analysis of well F05-01.

- **For DT, a value of 150 µs/ft has been assumed. The regression line suggests slowness values close to the sonic slowness of water (~180 µs/ft). That would imply shale particles in suspension, which seems to be unrealistic.**
- **For RHOB, a value of 2.02 g/cm^3 has been assumed.**

3.Appendices rock physics

Appendix K: Shear wave velocity prediction

In this appendix the estimated shear wave velocity values from well A15-04 are compared with Han's (1986) and Blangy's (1992) V_p-V_s relationships, and with the predicted shear wave velocities using Xu-White's (1995) clay-sand mixture model.

V_p-V_s relationship from well A15-04

Figure 15 presents the location of well A15-04.

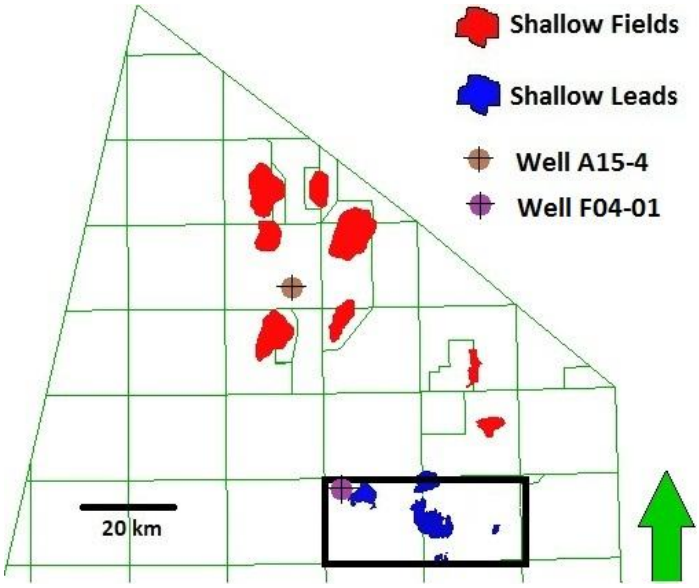

Figure 15: Shallow gas fields nearby (in red) and leads (in blue) within the study area. The area of interest is highlighted by the black box. Both wells A15-04 and F04-01 are shown.

Using the gamma ray cut-off described in section 5.1.2.2, two V_p-V_s relationships are derived for respectively shale (seals) and sand (reservoirs) in well A15-04. These relationships are shown in figure 16. As can be seen in the figure, the relationship corresponding to the fraction shale has a higher correlation coefficient than the V_p-V_s relationship for the sand fraction in well A15-04. Note that a depth interval of 500-1000 m (MD) has been used for this matter.

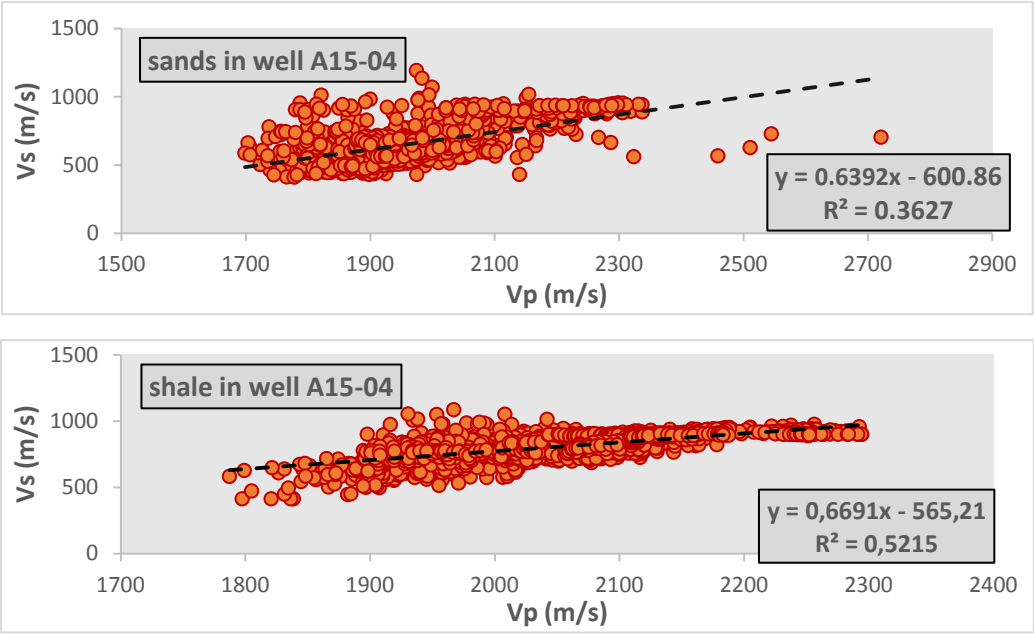

Figure 16: The derived V_p-V_s relationships in well A15-04 for both the sand fraction (above) and the shale fraction (below).

Comparison between the A15-04, Han's (1986) and Blangy's (1992) V_p-V_s relationships

The empirical relationships of Han and Blangy are derived for respectively consolidated and poorly consolidated sandstones. The following figure compares these two empirical relationships with the V_p-V_s relation derived from well A15-04 by applying it to the reservoirs in well F04-01, following the conditions mentioned in section 5.1.2.2:

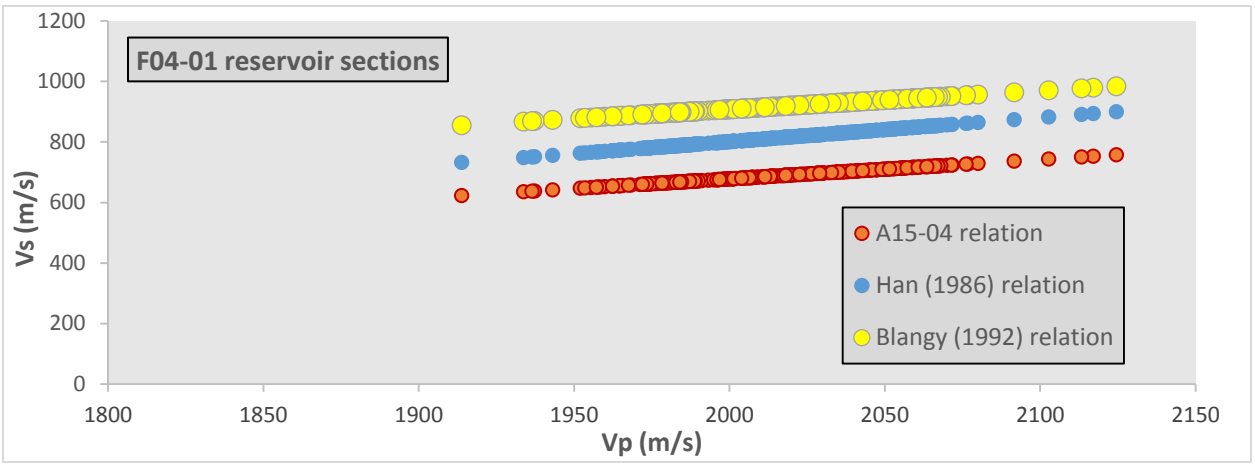

Figure 17: The results of the application of the two empirical relationships and the V_p-V_s relationship derived from well A15-04 on the reservoirs/sands in well F04-01.

The A15-04 relationship predicts systematically lower V_s values compared with the V_p-V_s relations from literature. An explanation may be the unconsolidated character of the sediments and the fraction shale in the shallow reservoirs within wells F04-01 and A15-04. Since the shale fraction at these shallow depths experienced only limited compaction, it is expected that they contain relatively large amounts of clay-bounded water which results in low seismic velocities. The obtained sands in well A15-04, after applying the mentioned gamma ray cut-off, are unconsolidated and probably still contain some shale. Thus it is likely that the derived V_p-V_s relationship, for sands/reservoirs, from well A15-04 is based on a mixture of unconsolidated sands and (some) shale that have lower seismic velocities than pure (consolidated) sandstones.

The A15-04 relation has approximately the same trend as Blangy's empirical relationship, as they both represent poorly consolidated sediments. At compressional wave velocities lower than 2584 m/s, Han's relation predicts lower V_s values than Blangy's relation. Han's (1986) relation is based on measurements of which the lowest observed V_p value was 3130 m/s, hence applying this relation to these low seismic velocities most likely results in large uncertainties. The two relationships from literature are in fact only applicable to the set of rocks which was studied.

Comparison between shear wave velocities predicted using the A15-04 relation and Xu-White's model

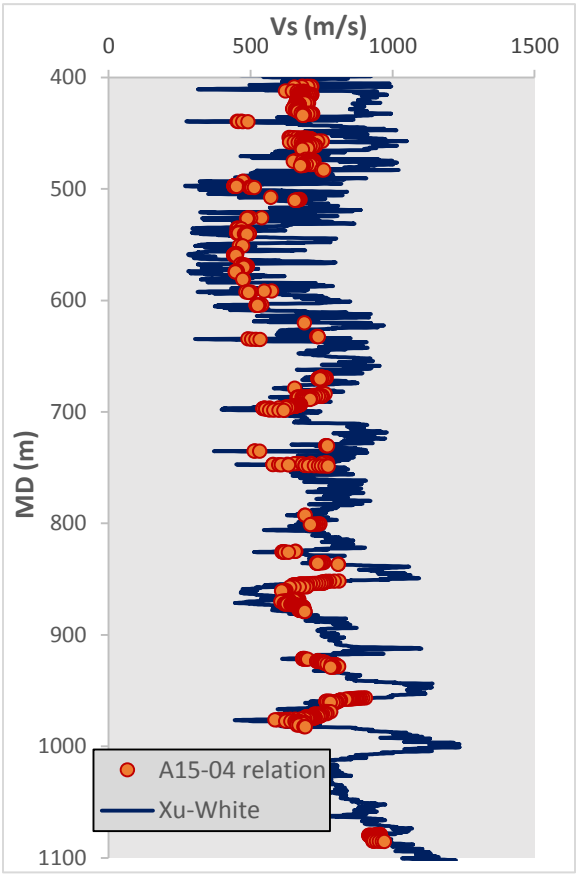

Figure 18: Comparison between predicted V_s values using Xu-White's method and the derived V_p-V_s relationship in well A15-04.

The above figure presents the comparison between shear wave velocity data predicted using the A15-04 relationships, for shale and sand separately, and using Xu-White's clay-sand mixture model which is described by Keys and Xu (2002). Most of the predicted V_s values, using A15-04 relationships, fall exactly on the V_s log derived with Xu-White's method.

Appendix L: Effective to total volume fraction conversion

Since in the petrophysical analysis the shale volume has been derived, the corresponding porosity is in fact the effective porosity. In order to predict V_s values with Xu-White's method, the volume fraction clay must be known; conversion between the effective system and the total system is required. This appendix shows the equations that are used in order to calculate the total porosity from the effective porosity.

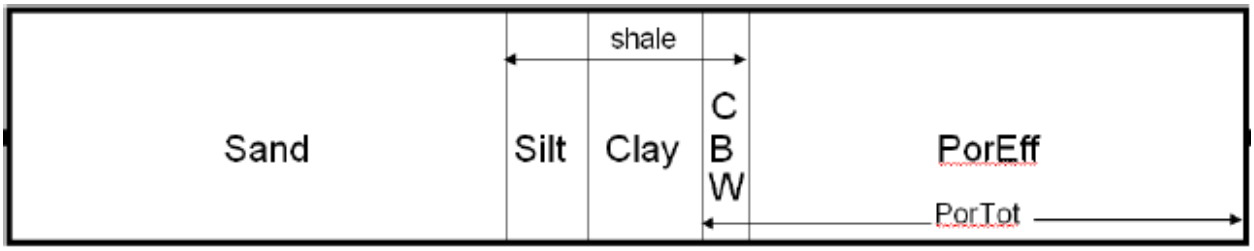

Figure 19: Schematic diagram showing the difference between the total and the effective system. In the effective porosity system the minerals sand and shale are used, whilst the clay mineral is used in the total porosity approach. Shale consists of silt, clay and clay-bounded water (CBW). The effective porosity considers only the free pore space where fluids can move freely; excluding clay-bounded water.

By grouping the silt contribution with the sand (as silt is electrically/chemically inert to sand), Connolly and Kemper (2007) define the following relation:

$$f_{\text{clay}} = f_{shale}(1 - \Phi_{shale}) \quad [1]$$

Where ϕ_{shale} and f_{shale} are respectively the shale porosity and the total mineral volume corresponding to shale. The total mineral volume can be converted to the volume fraction (V_x) by using the following equations:

$$V_{\text{clay}} = f_{clay}/(1 - \Phi_{total}) \quad [2]$$

$$V_{\text{shale}} = f_{shale}/(1 - \Phi_{effective}) \quad [3]$$

After substituting in equation [1] and some rearranging, we get:

$$V_{\text{clay}} = V_{\text{shale}}(1 - \Phi_{shale})(1 - \Phi_{effective})/(1 - \Phi_{total}) \quad [4]$$

This equation can be re-organized to:

$$1 - \Phi_{total} = 1 - \Phi_{effective} - CBW = 1 - \Phi_{effective} - f_{shale}\Phi_{shale} = 1 - \Phi_{effective} - (1 - \Phi_{effective})V_{\text{shale}}\Phi_{shale} = (1 - \Phi_{effective})(1 - V_{\text{shale}}\Phi_{shale}) \quad [5]$$

The above equation presents the relation between the total and the effective porosity. In order to convert the volume fraction shale to the volume clay, we substitute equation [5] in equation [4]:

$$V_{\text{clay}} = V_{\text{shale}}(1 - \Phi_{shale})/(1 - V_{\text{shale}}\Phi_{shale}) \quad [6]$$

Since V_{shale} is known, the only parameter left, in order to convert V_{shale} to V_{clay} and vice versa, is ϕ_{shale}.

The determination of ϕ_{shale} requires the densities of clay, shale and the bound-water and is given by the following formula:

$$\Phi_{shale} = (\rho_{clay} - \rho_{shale})/(\rho_{clay} - \rho_{bound-water}) \quad [7]$$

In these equations the $\rho_{bound\text{-}water}$ is hard-wired to 1.0 g/cm^3. The densities used for clay and shale are constant values as presented in table 5.3 (section 5.1.4), which seems a valid assumption since only a small interval is analyzed here.

Figure 20 presents the effective and total porosity system for well F04-01.

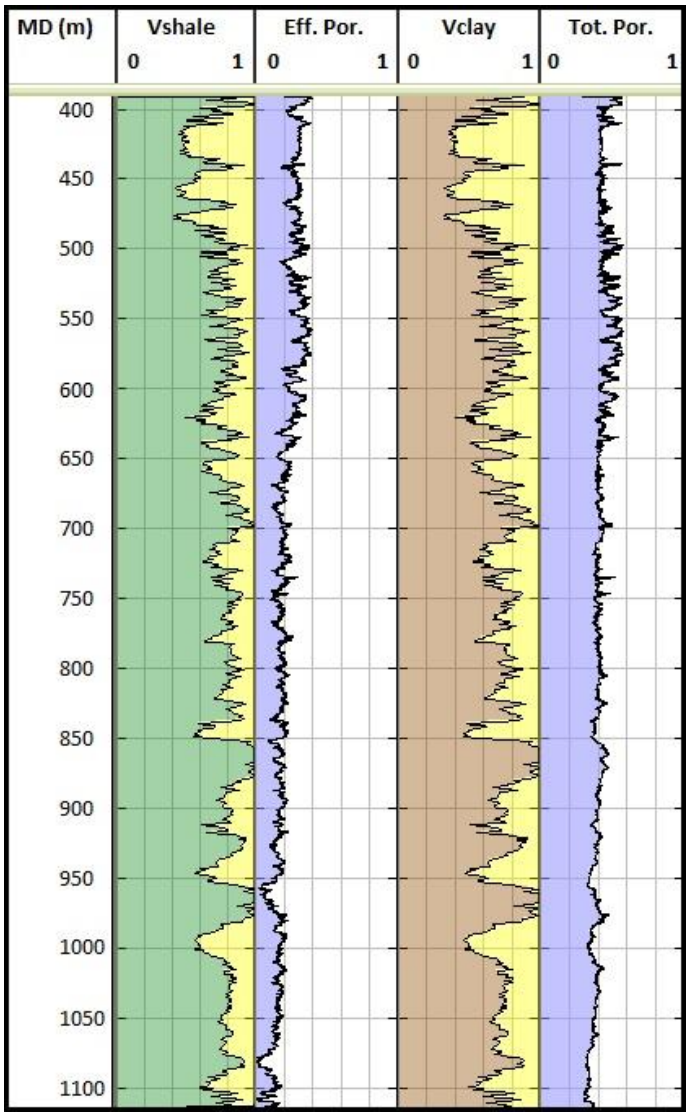

Figure 20: The effective porosity system, obtained from the petrophysical analysis, and the total porosity system, which has been derived using the equations in this appendix, for well F04-01. The volume fractions of shale, quartz and clay are respectively shown in green, yellow and brown. The densities used for clay and shale are shown in table 5.3 (section 5.1.4).

Appendix M: Salinity of sodium chloride in well MKP-14

This appendix provides additional information about the salinity measurement in well MKP-14. The salinity is a required parameter in order to predict elastic properties for brine using Batzle and Wang's (1992) method. Figure 21 presents the location of well MKP-14.

Figure 21: The location of both wells F04-01 and MKP-14. The salinity measurement in well MKP-14 is used in order to derive brine properties with Batzle and Wang's method.

Table 1: The salinity measurement in well MKP-14.

Well	MD (m)	TVD_{ss} (m)	Cl (ppm)	NaCl (ppm)	NaCl (fraction)	Temperature (°C)	Source
MKP-14	794.3	776.3	46000	75670	0.076	16	Water analysis (RFT)

The repeat formation tester (RFT) is designed to measure formation pressures quickly and accurately at specific points on the borehole wall. Using this tool, fluid samples from the formation can also be taken and being analyzed. In this particular case, the chloride concentration was obtained during the water analysis. Crain (2000) provides an equation which derives the water salinity in parts per million NaCl from the measured chloride content in parts per million:

$$S_{NaCl} = S_{Cl} * 1.645 \quad [8]$$

where S_{NaCl} and S_{Cl} are the water salinities in respectively ppm NaCl and ppm Cl. Note that this relationship is for pure NaCl solutions and the factor may be higher or lower if other ions are present. The obtained salinity in fraction NaCl is shown in table 1.

Although the water analysis was performed on a sample which was taken outside the study area from a depth of ~775 m, it is assumed that the same salinity occurs in brine in the identified water-bearing reservoir in well F04-01 since it is the only measurement available.

Appendix N: Coefficients ω_{ij} in V_W formula (Batzle and Wang, 1992)

The table below presents the coefficients for ω_{ij} that are used in the V_W formula derived by Batzle and Wang (1992).

Table 2: The coefficients for ω_{ij}.

Coefficient	Value	Coefficient	Value
ω_{00}	1402.85	ω_{02}	$3.437*10^{-3}$
ω_{10}	4.871	ω_{12}	$1.739*10^{-4}$
ω_{20}	-0.04783	ω_{22}	$-2.135*10^{-6}$
ω_{30}	$1.487*10^{-4}$	ω_{32}	$-1.455*10^{-8}$
ω_{40}	$-2.197*10^{-7}$	ω_{42}	$5.230*10^{-11}$
ω_{01}	1.524	ω_{03}	$-1.197*10^{-5}$
ω_{11}	-0.0111	ω_{13}	$-1.628*10^{-6}$
ω_{21}	$2.747*10^{-4}$	ω_{23}	$1.237*10^{-8}$
ω_{31}	$-6.503*10^{-7}$	ω_{33}	$1.327*10^{-10}$
ω_{41}	$7.987*10^{-10}$	ω_{43}	$-4.614*10^{-13}$

Appendix O: Berryman's theoretical approach

Berryman's adapted bounds are given by Mavko et al. (1998):

$$K_{HS+} = \Lambda(\mu_{max}) \quad [9]$$

$$K_{HS-} = \Lambda(\mu_{min}) \quad [10]$$

$$\mu_{HS+} = \Gamma\big(\zeta(K_{max}, \mu_{max})\big) \quad [11]$$

$$\mu_{HS-} = \Gamma\big(\zeta(K_{min}, \mu_{min})\big) \quad [12]$$

where

$$\Lambda(z) = < \frac{1}{K_{(r)} + \frac{4}{3}z} >^{-1} - \frac{4}{3}z \quad [13]$$

$$\Gamma(z) = < \frac{1}{\mu_{(r)} + z} >^{-1} - z \quad [14]$$

$$\zeta(K, \mu) = \frac{\mu}{6}\left(\frac{9K + 8\mu}{K + 2\mu}\right) \quad [15]$$

and μ_{min}, μ_{max}, K_{min} and K_{max} are respectively the minimum and maximum values for the shear and bulk modulus corresponding to the individual constituents. The symbol <·> indicate an average over the components weighted by their volume fractions. The lower bound of Berryman's approach (K_{HS-} and μ_{HS-}) may be used to predict the effective elastic moduli for unconsolidated sediments consisting of more than two components. This has been applied to the identified water-bearing reservoir in well F04-01, and results are shown below.

For this calculation it is assumed that the volume fraction quartz and shale are equal to respectively 0.55 and 0.45. The average effective porosity within the analyzed interval equals 0.31. Together with the elastic properties of brine, quartz and shale (tables 5.2 and 5.3), Berryman's approach can be used to predict the Hashin-Shtrikman lower bound for a quartz-shale-brine mixture. Attention is paid to the lower bound only since the sediments of interests are unconsolidated.

μ_{min} = 0 GPa μ_{max} = 31.46 GPa K_{min} = 2.57 GPa K_{max} = 38.59 GPa

$$K_{HS-} = \Lambda(0) \quad [16]$$

$$K_{HS-} = \left[\frac{\phi}{2.57} + \frac{(1-\phi)0.55}{38.59} + \frac{(1-\phi)0.45}{9.35}\right]^{-1} \quad [17]$$

$$K_{HS-} = \mathbf{6.11\ GPa} \quad [18]$$

$$\mu_{HS-} = \Gamma\big(\zeta(2.57,0)\big) \quad [19]$$

$$\zeta(2.57,0) = 0 \text{ GPa} \quad [20]$$

$$\mu_{HS-} = \Gamma(0) \quad [21]$$

$$\mu_{HS-} = \mathbf{0\ GPa} \quad [22]$$

4.Appendices AVO modelling

Appendix P: Normal distributions for V_p, V_s and ρ for seal and reservoir with varying gas saturation

This appendix presents the normal distributions of the three elastic properties per gas saturation for both seal and reservoir.

0% gas

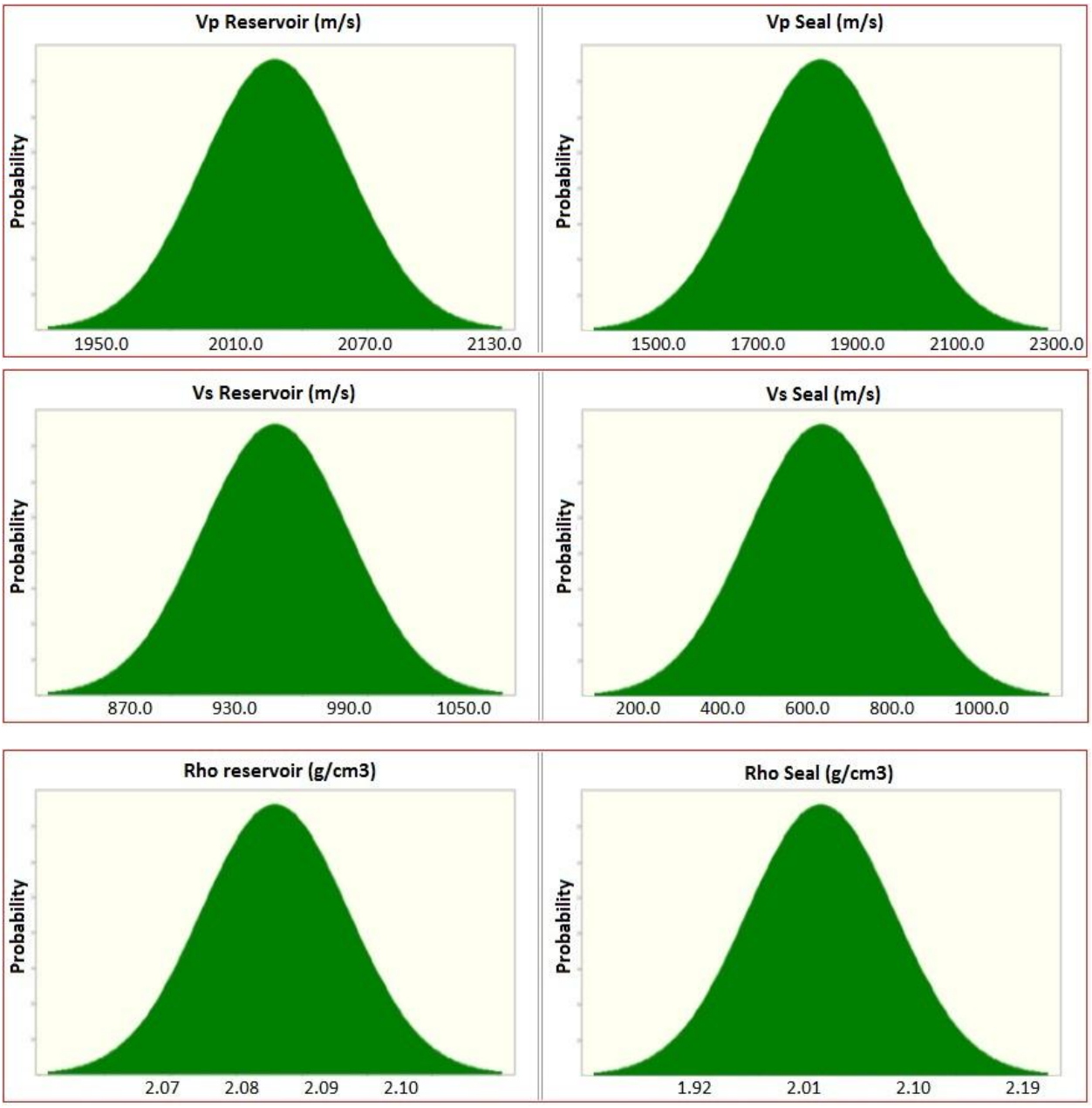

Figure 22: Normal distributions for the elastic parameters for the water-bearing case.

1% gas

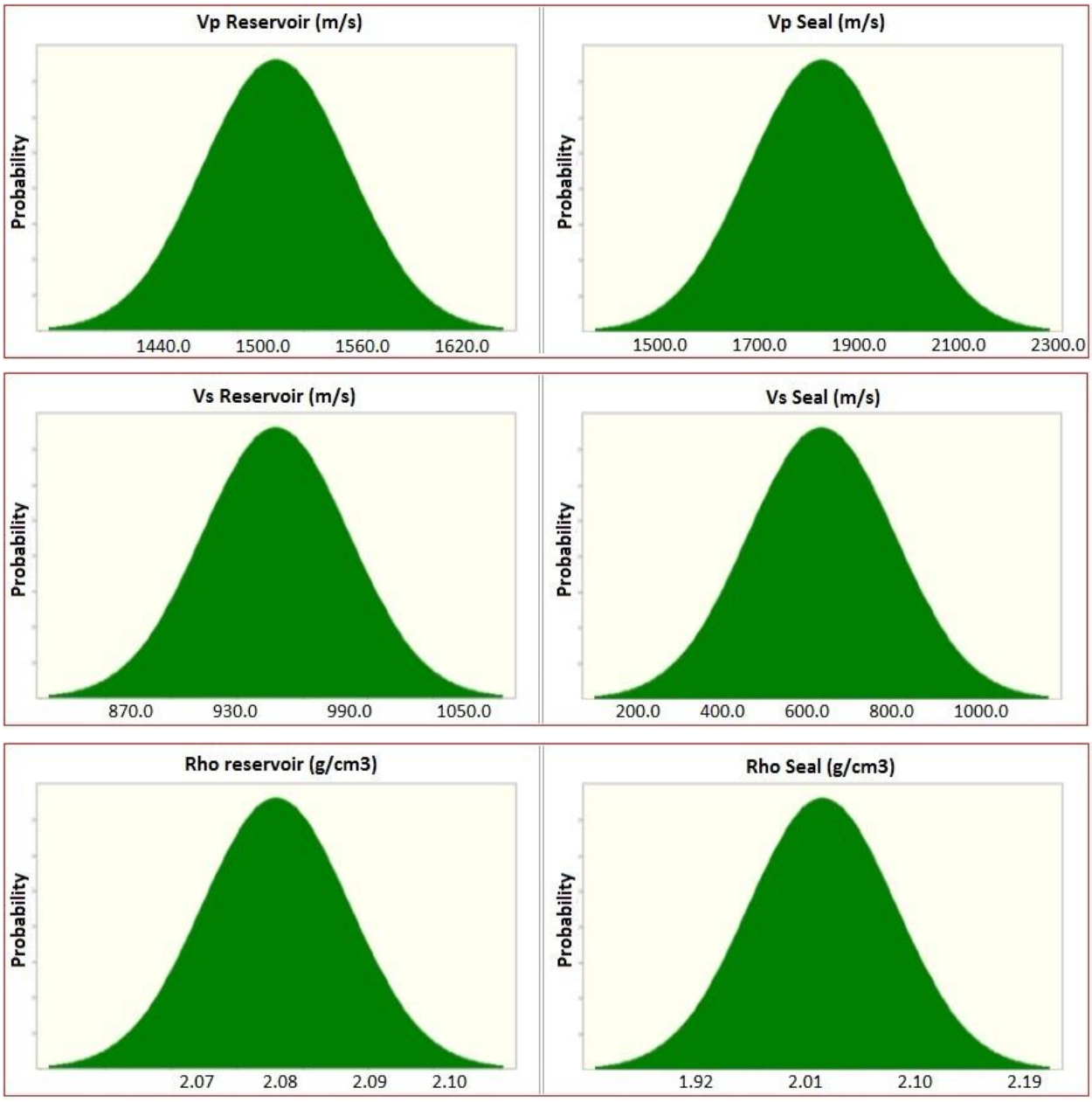

Figure 23: Normal distributions for the elastic parameters for a gas saturation of 1% within the reservoir.

100% gas

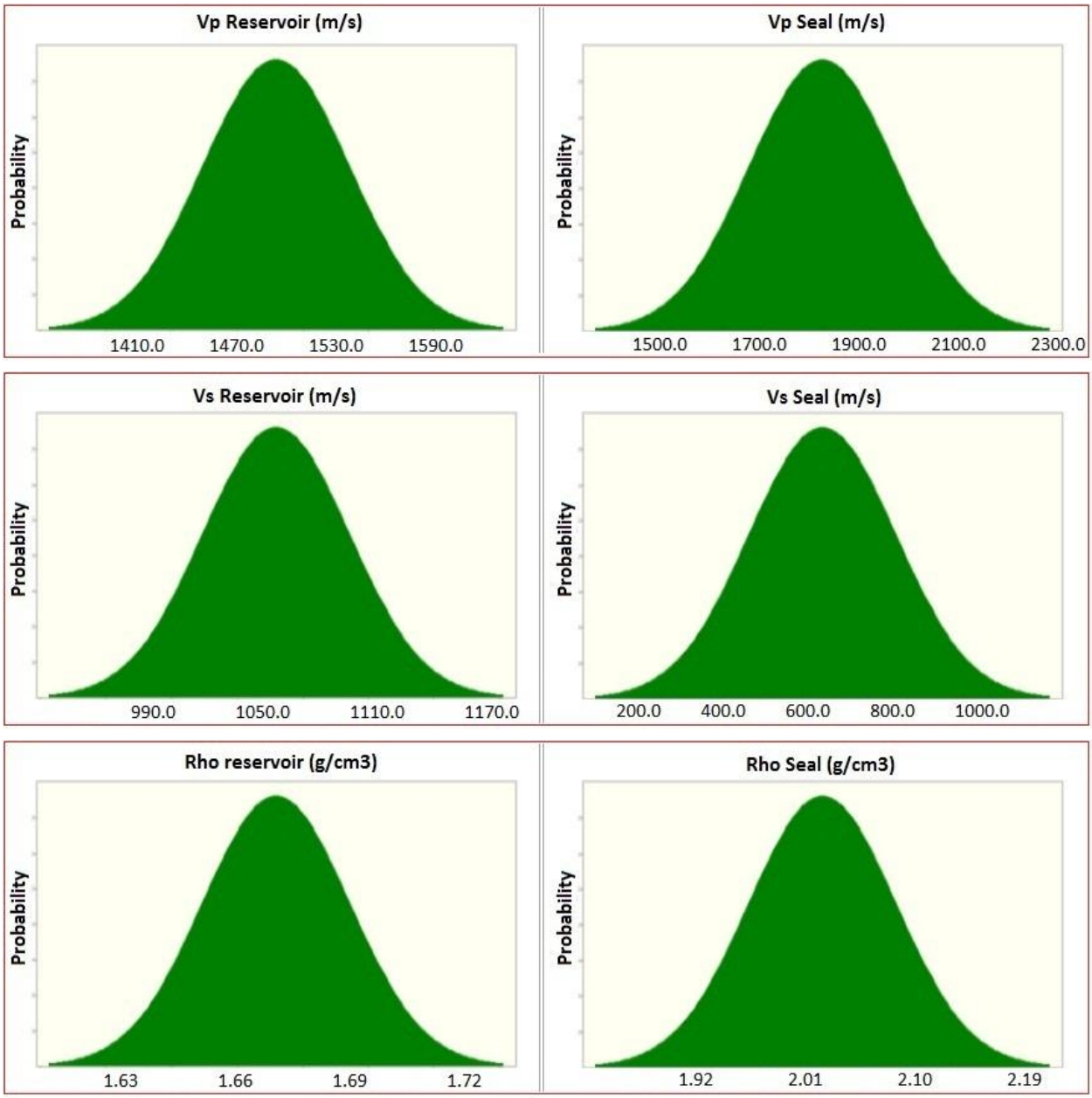

Figure 24: Normal distributions for the elastic parameters for a gas saturation of 100% within the reservoir.

Appendix Q: Conversion of 100% gas- to 100% water-bearing

In figure 6.6 (section 6.3), 4 out of 1000 situations show positive gradients with respect to a gas saturation of 100%. The elastic properties corresponding to the black AVO trend in figure 6.6 are converted to elastic parameters with respect to gas saturations of 0%, 1% and 20%. Gassmann's algorithm (total porosity approach) has been used for this. For this calculation a total porosity of 0.41, a V_{shale} of 0.45 ($V_{dry\ clay}$ of 0.4) and a V_{quartz} of 0.6 was assumed. The results, which are the elastic properties corresponding to the reservoir, are shown in table 3. Note that the elastic parameters for the seal, which were used in order to construct the black AVO trend in figure 6.6, remain constant. The same mineral and fluid properties are assumed as shown in tables 5.2 and 5.3.

Table 3: The elastic properties corresponding to gas saturations of 0%, 1%, 20% and 100%.

Gas saturation in reservoir	V_p (m/s)	V_s (m/s)	ρ (g/cm^3)
0%	2071.8	913.2	2.001
1%	1505.1	914.1	1.997
20%	1336.2	932.7	1.918
100%	1473.0	1037.2	1.663

	V_p (m/s)	V_s (m/s)	ρ (g/cm^3)
Seal	1937.6	1101.0	2.04

With the Zoeppritz equations, reflection coefficients per angle of incidence are calculated for the different gas saturations in the reservoir. These results are shown in figure 6.7 (section 6.3.1).

Appendix R: Intercept-gradient values for the average modelling results

This appendix shows the derivation of the intercept and gradient values that correspond to the average modelling results (the bold lines in figures 6.5 and 6.6; section 6.3). In order to obtain the intercept and gradient values, only angles of incidence of 0°-35° should be used due to the two-term Shuey assumption. In figure 25 the modelled reflection coefficients are plotted as a function of the squared sine of the angle of incidence. A linear fit has been applied through the reflectivities using angles of incidence up to 35°. The obtained intercept and gradient values are also presented in this plot (see figure 2.12, section 2.4.2 for more information).

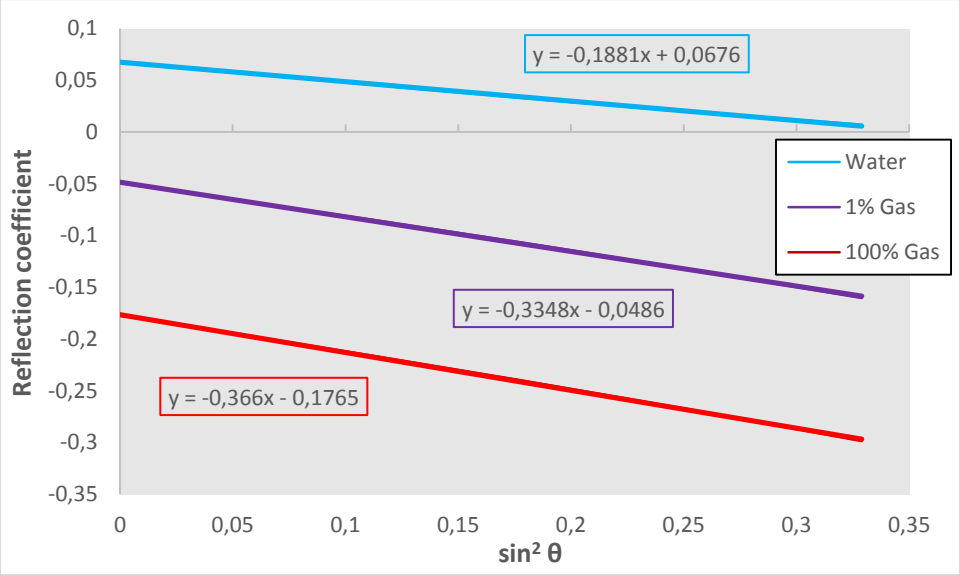

Figure 25: The derivation of the intercept and gradient values for the average modelling results for gas saturations, within the reservoir, of 0%, 1% and 100%.

Subsequently, these intercept-gradient combinations are plotted in an intercept-gradient cross plot shown in figure 6.8 (section 6.3.2).

5.Appendices pre-stack data analysis

Appendix S: Variation in angles of incidence per trace in lead F04-P1

The angle of incidence per seismic trace slightly varies per location within the two analyzed areas shown in figure 7.5 (section 7.2.1). This appendix shows this discrepancy in incidence angles per seismic trace for both areas 1 and 2 in lead F04-P1. Figure 26 presents the distribution of the angle of incidence in the two analyzed areas.

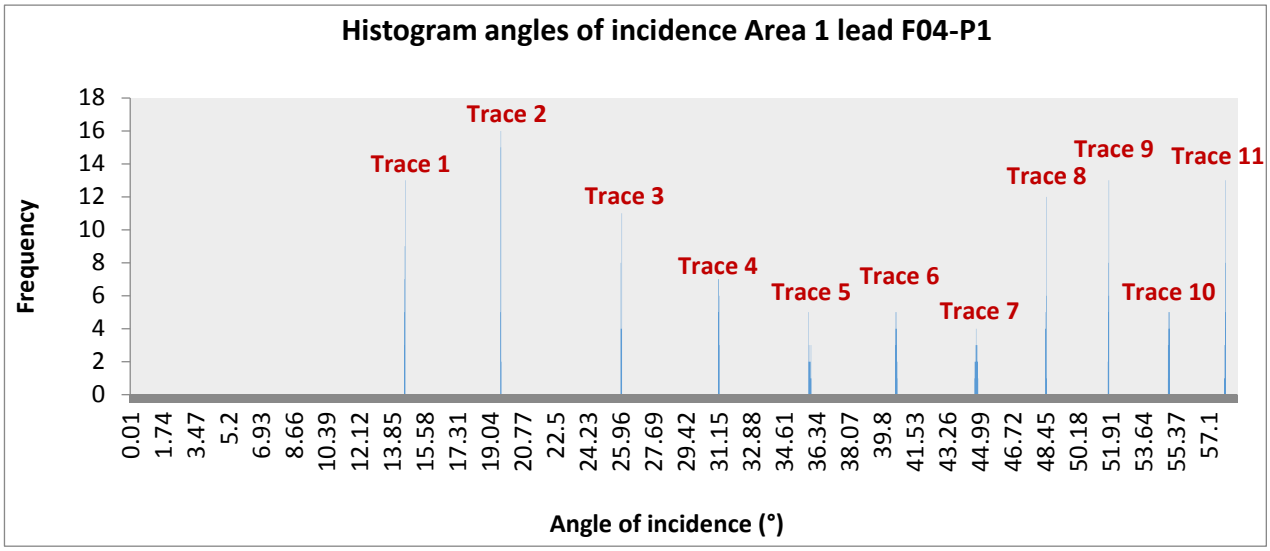

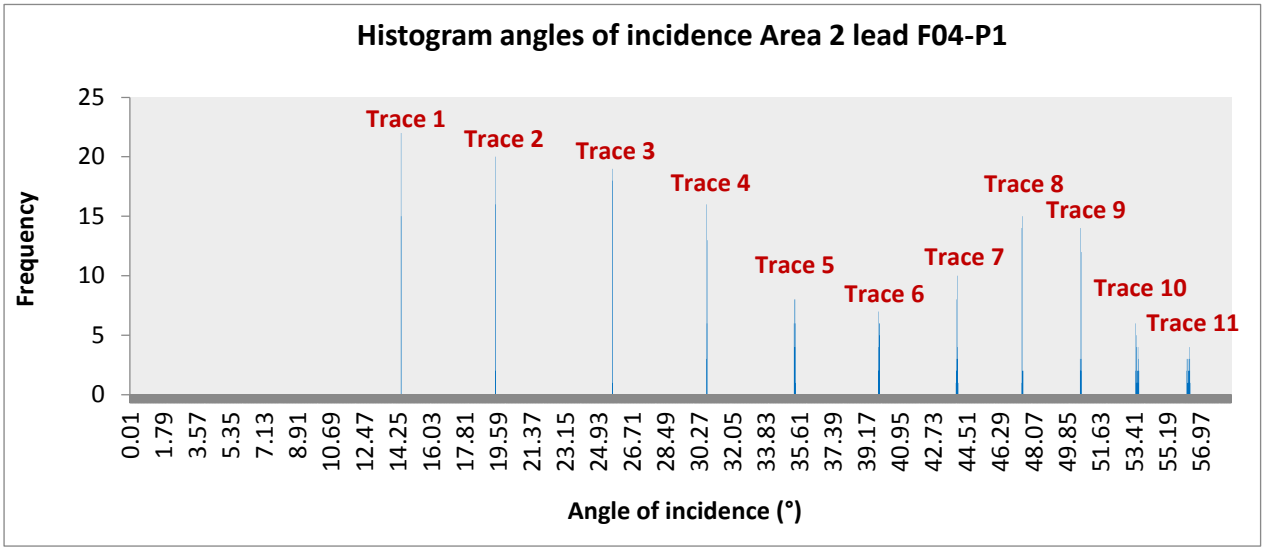

Figure 26: The histograms which presents the distribution of the angle of incidence in area 1 (above) and area 2 (below) in lead F04-P1.

The histograms show that there is very little variation in the angle of incidence per seismic trace. This variation is neglected during further analysis of other anomalies due to time limitations. In the analysis of lead F04/F05-P1 constant angles per trace are assumed in area 1 and area 2 separately.

Appendix T: Intercept-gradient values in leads F04-P1 and F04/F05-P1

This appendix shows the derivation of the intercept and gradient values for both the water- and gas-bearing sediments in leads F04-P1 and F04/F05-P1. In order to obtain the intercept and gradient values, only angles of incidence of 0°-35° should be used due to the two-term Shuey assumption. Figure 27 shows the amplitude versus $\sin^2 \theta$ plots for both leads. The intercept and gradient values, for areas 1 and 2 in both leads, are also presented in these plots (see figure 2.12, section 2.4.2 for more information).

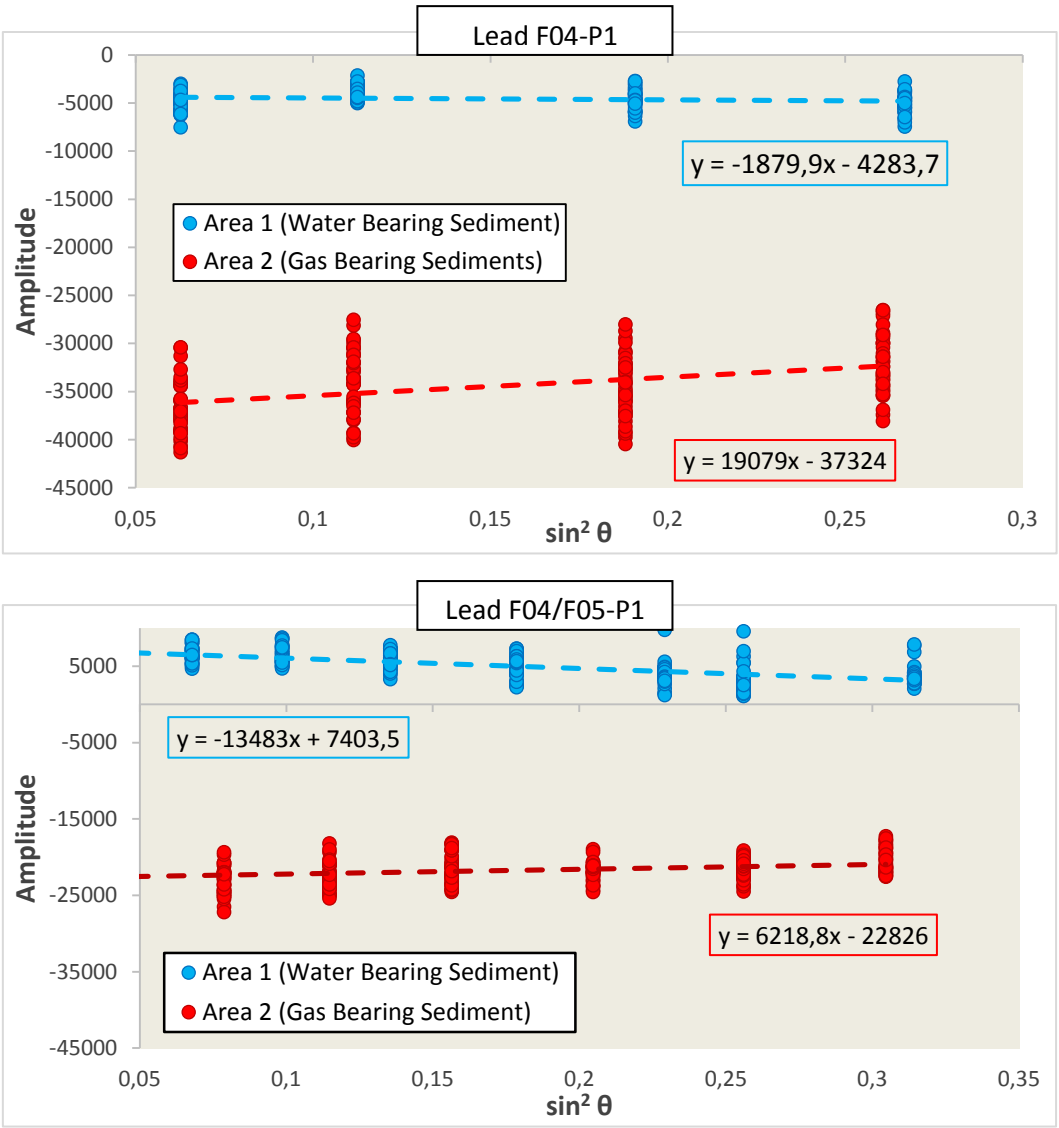

Figure 27: The amplitude versus $\sin^2 \theta$ plots for both lead F04-P1 (above) and lead F04/F05-P1 (below). The obtained intercept-gradient combinations are plotted in the intercept-gradient cross plot shown in figure 7.15, section 7.2.3.

Appendix U: Modelled tuning thickness

As the modelled shale layer, with sufficient sealing capacity, contains a thickness of approximately 5 m, one should ask the question whether this sealing layer can be identified on seismic data. The theory behind the tuning effect has been discussed in section 2.1.4. This appendix shows the modelled tuning thickness for the relatively thin shale layer that has been identified as a seal in well F04-01.

In this tuning wedge model the average sets of elastic parameters for seal and reservoir for water-bearing conditions are used (see table 5.6; section 5.3.4). It is assumed that the reservoir conditions corresponding to 0% gas also occur above the thin shale layer. The wavelet used in this model is the extracted wavelet from the full-stack seismic cube. Note that this wavelet is converted to the US polarity convention (increasing impedance yields positive amplitudes). The modelled amplitudes, using the Zoeppritz equations for $R_{pp,}$ are stacked from 0° to 40°. Figure 28 presents the tuning wedge model.

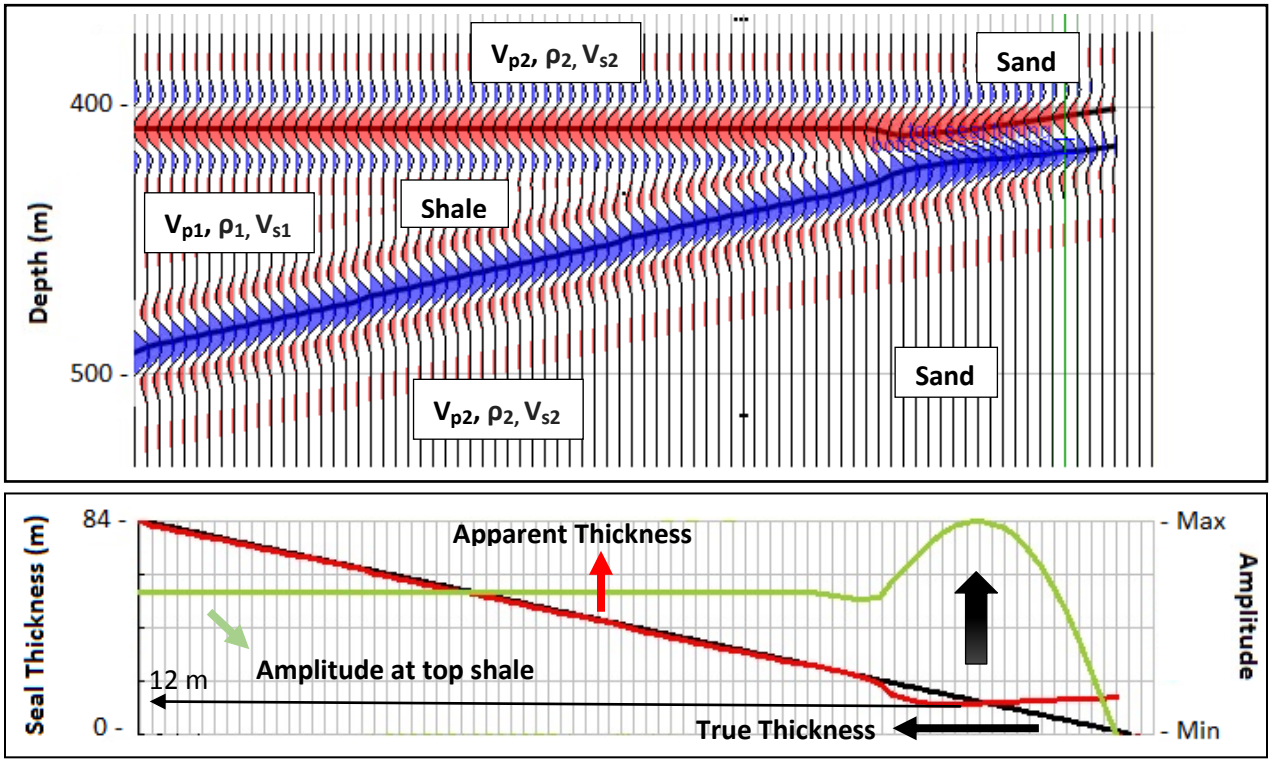

Figure 28: The tuning wedge model for the used shale properties. According to this model, the tuning thickness is approximately 12 m (marked by the black arrow in the lower graph). The modelled shale layer, which acts as a seal, is more or less 5 m thick. It is very likely that the thin shale layer is not recognizable on full-stack seismic data, as the apparent thickness remains ~12 m and the true thickness may be much less. The following rock properties were used (table 5.6): V_{p2} = 2027.7 m/s, V_{s2} = 946.5 m/s, ρ_2 = 2.084 g/cm^3, V_{p1} = 1826.3 m/s, V_{s1} = 619.9 m/s and ρ_1 = 2.018 g/cm^3. This model is made using RokDoc software.

The above figure shows that, according to this tuning wedge model, shale thicknesses of less than approximately 12 m are not recognizable on full-stack seismic data. Note that in this model the average sets of elastic parameters are used, for both the seal and reservoir, for water-bearing conditions. The tuning thickness corresponding to the reservoir also equals 12 m, assuming the same properties as in figure 28.